

# NATIONAL AIR INTELLIGENCE CENTER



DTIC QUALITY INSPECTED 4

THE MEASUREMENT OF A HIGH-POWER CO<sub>2</sub> LASER'S  
FAR-FIELD OUTPUT INTENSITY DISTRIBUTION

by

Jang Lijang



Approved for public release:  
distribution unlimited

19960618 156

**HUMAN TRANSLATION**

NAIC-ID(RS)T-0146-96 22 April 1996

MICROFICHE NR: 96 C 000 342

THE MEASUREMENT OF A HIGH-POWER CO<sub>2</sub> LASER'S  
FAR-FIELD OUTPUT INTENSITY DISTRIBUTION

By: Jang Lijang

English pages: 15

Source: Jiguang Jishu (Laser Technology), Vol. 14, Nr. 1,  
February 1990; pp. 39-44

Country of origin: China

Translated by: Leo Kanner Associates  
F33657-88-D-2188

Requester: NAIC/TATD/Bruce Armstrong

Approved for public release: distribution unlimited.

THIS TRANSLATION IS A RENDITION OF THE ORIGINAL  
FOREIGN TEXT WITHOUT ANY ANALYTICAL OR EDITO-  
RIAL COMMENT STATEMENTS OR THEORIES ADVOC-  
ATED OR IMPLIED ARE THOSE OF THE SOURCE AND  
DO NOT NECESSARILY REFLECT THE POSITION OR  
OPINION OF THE NATIONAL AIR INTELLIGENCE CENTER.

PREPARED BY:

TRANSLATION SERVICES  
NATIONAL AIR INTELLIGENCE CENTER  
WPAFB, OHIO

#### GRAPHICS DISCLAIMER

All figures, graphics, tables, equations, etc. merged into this translation were extracted from the best quality copy available.

# The Measurement of a High-Power CO<sub>2</sub> Laser's Far-Field Output Intensity Distribution

Jang Lijang

(Gulin Institute of Optical Communication)

**Abstract:** An experimental method for measuring the far-field intensity distribution of a TE CW CO<sub>2</sub> laser beam by two dimensional scanning is described. The reliability and practicability of the measurement system have been discussed in details. The measurements of a TE CW CO<sub>2</sub> laser with 2 kW output are given.

## 1. Preface

The far-field intensity distribution of a laser beam is one of the most important indicators of laser beam quality. Therefore, how to precisely measure the far-field intensity distribution of the high-power laser beam has become a vital key to high-power laser device application. Noticeably, the high-power laser beam, due to its high power density, its complex model structure and its optical path distribution which is no longer an ideal Guassian distribution, can hardly be measured accurately with conventional methods.

Take the shooting method [1] as an example, it uses a calibrated recording medium to record the configuration of far-field beam intensity distribution. However, when laser power density is high, the mechanism of laser-substance interaction turns out to be so complicated that all kinds of intricate phenomena will take place on the surface of the irradiated medium, such as light absorption, reflection, scattering, thermal conduction, liquidation, vaporization, spray, etc. Thus, it is apparently impractical to simply consider the radiation track as

the optical field distribution.

On the other hand, one-dimensional scanning [2], although providing relatively reliable measurements, can only measure beam distribution on a particular cross section. Nevertheless, for those beams with complicated far-field distribution and without symmetry, laser beam distribution on a specific cross section, in general, cannot reflect the full view of the far-field beam distribution. Once again, it is genuinely difficult to determine, within the mere few seconds of laser device working time, which cross-section the beam distribution comes from.

Also, the variable diaphragm method [3], as well as other methods which take far-field distribution as Gaussian distribution, are apparently no longer applicable because they require the measured flare to be axially symmetrical and have Gaussian distribution.

The two-dimensional scanning method that we use can basically overcome the shortcomings existing in the above-mentioned measurement methods.

In principle, this method can be applied in measurement of output beam far-field distribution from different laser devices. Specifically this method has unique features, namely, it uses a rotary cylinder with numerous small holes distributed in accordance with spiral rule to replace the one-dimensional scanning device, without changing the location of the laser beam and detector, and finally completes the two-dimensional scanning with one dimensional rotating process so as to measure spatial distribution of the optical field. Its technical setup is used to measure the 2 kW level TE CW CO<sub>2</sub> laser beam, the measurements of which will be discussed later in this paper.

## 2. Measurement Mechanism and Experimental Equipment

The Far-field laser distribution refers to beam intensity distribution shown on the screen at an infinite point, namely the Fraunhofer diffraction pattern. In actual measurement, the laser beam can be observed on the focal plane of focalizer after being focalized.

The measurement setup is indicated in Fig. 1. The laser beam, after being attenuated, is transmitted first into the reflector focusing system to be focused, and then into the scanning cylinder, in which the beam is reflected to its internal wall through a reflector, and finally it goes through the scanning process by the scanner. After that, the scanned beam signal is received by a thermovoltaiic infrared detector, and then is transferred to the storage oscillograph for display. The experiment result can be recorded by an oscillography camera. The He-Ne tube, beam-expansion telescope, internal focalization telescope as well as optical power meter in the experimental system are all used exclusively for optical path adjustment and power observation.

The scanning principle is shown in Fig. 2. It can be seen that there are numerous small holes spreading in a spiral form on the scanning cylinder, in which, axial spacing among holes, hole diameter, as well as the center angle between two adjacent holes are all determined by the measured flare size. Normally, when the scanning cylinder performs scanning at a certain rotational speed over the measured flare, every small wave on the scanning curve recorded by oscillograph under the coordinate indicated in Fig. 2 signifies the y-direction relative distribution of light intensity on a particular cross section in X direction. Whereas the envelope on the scanning curve simply represents the light intensity distribution in X axis. Again, with the scanning curve and scanning time (t) recorded in the experiment, a three-

dimensional graph [1] of the far-field light intensity distribution can be easily generated.

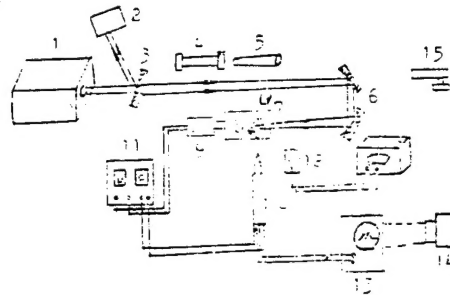


Fig. 1. Schematic diagram of the measurement device for laser beam intensity far-field distribution

Key: 1. TE CO<sub>2</sub> laser device; 2. Laser absorption device; 3. Laser attenuator; 4. He-Ne laser device; 5. Beam expansion telescope; 6. Focusing system; 7. Scanning cylinder; 8. 45° optical reflector; 9. SZ 61 direct current servo motor; 10. Thermo-voltaic infrared detector; 11. Direct current voltage regulator; 12. Laser power meter; 13 PM-3266 Memory oscillator; 14. Oscilloscope camera; 15. Internal focalization telescope

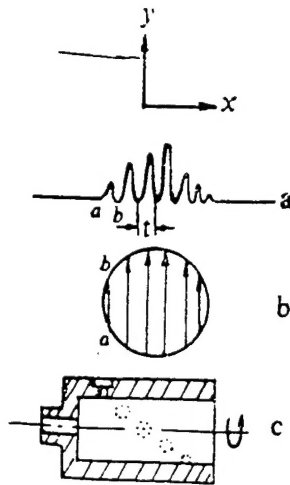


Fig. 2. Schematic diagram of scanning principle

Key: a - Curve recorded in experiment  
 b - Measured flare  
 c - Scanning cylinder



Technically, to measure optical field distribution of the continuous high-power laser beam, the following problems must be solved: (1) beam attenuation without distortion; (2) image error correction of focusing system; (3) matching between scanning cylinder rotating speed and detector response time; and (4) optical path adjustment. Further discussion in this respect is as follows:

#### 1. Beam Attenuation without Distortion

As the light detector can only measure limited energy, the high energy laser beam has to be attenuated before being detected by the detector. As a result, the attenuator used during measurement should attenuate laser power intensity to a required value without changing the far-field laser beam distribution, and at the same time, maintain its capability of withstanding high-energy laser beam radiation.

In addition, as two-dimensional sampling theory suggests [1], far-field distribution of any beam passing through the raster, as long as its divergence angle is less than  $\lambda/d$ , is a square matrix made of a series of separated flares, with  $\lambda/d$  as their spacing respectively in  $x$ ,  $y$  direction. It also undoubtedly proves that optical field distribution  $I_{mn}$  of flare in column  $n$  and row  $m$  in the square matrix and the non-attenuated beam far-field distribution  $I_0$  are in geometric similarity. Thus, the hole diffraction raster constituted by a series of  $m \times n$  holes arranged at a certain spacing  $b$  is an ideal attenuator, whose structure is shown in Fig. 3.

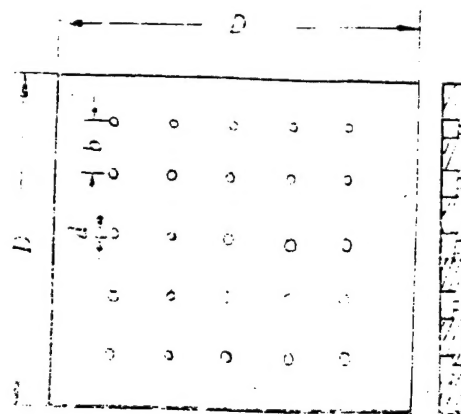


Fig. 3. Structure schematic diagram of raster attenuator

This kind of attenuator can perform two major attenuating functions. First, since most beams incident upon the front face of the raster can only pass through the holes, when beam diameter is much larger than hole diameter, the relation between overall light flux output from the raster and total light flux incident upon the raster can be expressed as follows:

$$\omega_{\text{output}}/\omega_{\text{input}} = \pi d^2/(4b) \quad (1)$$

where  $b$  is spacing between two holes, and  $d$  is hole diameter. Obviously, properly choosing the size of  $b$  and  $d$  can ensure a desired attenuation effect. Secondly, due to mutual interference between beams, far-field distribution of the beam penetrating raster is made of a series of separated flares. In the case that an aperture is placed in the focal plane of the focalizer to permit only diffractive flare of a particular order to get through, the goal of secondary attenuation can be reached. Raster attenuator is characterized by the capability of withstanding enormous incident beam power density, reliable and stable working conditions, as well as a wide range of the receiving area. However, it can only be applied when divergence

angle is less than  $\lambda/d$ , and is difficult to process otherwise.

Among other things, an infrared parallel optical flat, coated by film with a certain penetrating capability to achieve attenuation, is another commonly used attenuator. It enjoys the feature of convenience in use, and its reflected light is available for other measurements. Yet its disadvantage is equally obvious, namely its aperture plate may distort transmitted light under the action of the high energy laser beam, for which cooling measures are necessary. In our experiment, ZnSe aperture plate with a 15% penetrating rate was used, along with a wind and water cooling process.

## 2. Image Error Correction of Focusing System

In the case that a single-sided focalizer is used, the focalizer is mounted at an angle of  $45^\circ$  to the optical path to create a  $45^\circ$  included angle between incident light and optical axis of focalizer. When He-Ne light is used to make an optical path adjustment, it is found that an ideal circular spot might not be obtained on the focal plane of the focalizer but a bright line with a dip angle. Whereas near the focal plane, there are respectively an ellipse with long radius parallel to the arc vector and an ellipse with long radius vertical to the arc vector, as indicated in Fig.4.

To make a correction of astigmatic aberration, two reflectors with mutually vertical optical axes and identical focusing distance are used to compensate one another so as to acquire the desired circular spot near the focal plane of the second reflector focalizer. This approach was adopted in our experiment and attained a smaller image error.

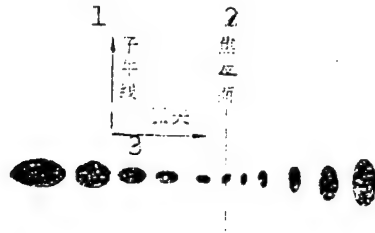


Fig. 4. Astigmatism generated image scattering when light transmits into condenser lens at  $45^\circ$  angle

Key: 1. Meridian; 2. Focal plane;  
3. Quantity vector

### 3. Selection of Various Parameters of Scanning Cylinder and Matching between Its Rotating Speed and Detector Response Time

The size of holes in the scanning cylinder should be determined in consideration of two aspects. To meet measurement precision, holes should be made as small as possible, to ensure that the wave shape of each hole represents distribution of a particular cross section along x direction. Nevertheless, excessively small hole size is not desirable for two reasons: first, it will create a difficulty in processing; secondly, it may lead to diffraction effect.

In our experimental equipment, hole size was selected as 0.7 mm. In addition, to ensure measurement accuracy, axial distance between the first and last holes, and the projection length of the arc line at any two adjacent holes on the cylinder cross section are required to be slightly larger than measured flare diameter. Thus, the inner diameter of the cylinder was designed as ID 78 mm, outer diameter OD 80 mm; axial spacing between two adjacent holes, 0.5 mm, and the center angle between them is  $15^\circ$ . In addition, to identify every frame signal, the center angle between the first and last holes was made to be  $60^\circ$ , and there were a total of 21 small holes on the cylinder.

The detector response time is required to be at least much larger than millisecond level to make measurement precision possible. In the case of  $10.6\ \mu\text{m}$  infrared light, there is a large selection of detectors. HgCdTe features fast response time (microsecond level) but has rather small photosensitive surface, while comparatively, the lithium tantalate thermovoltaic detector has slower response time (millisecond level) but larger photosensitive surface to withstand stronger light power density.

In making measurements over optical field distribution of a high energy laser beam, attenuation of light energy density poses a major concern. Therefore, we selected the thermovoltaic detector. Besides, compared with the HgCdTe detector, the working condition that thermovoltaic detector requires are much less demanding, i.e. it can work at room temperature with low cost and wider range of linear operation. Another significant advantage that this device shows is that it can capture different response times by making an adjustment to matched resistance in its operating electric circuit. The operating electric circuit we used for our detector is shown in Fig. 5, in which its response time is 2.04 ms. Upon the determination of the detector, rotating speed of the scanning cylinder could be decided accordingly. To achieve its synchronization with oscillograph signal, the rotating speed was designed as 400 RPM following a comparison in the experiment.

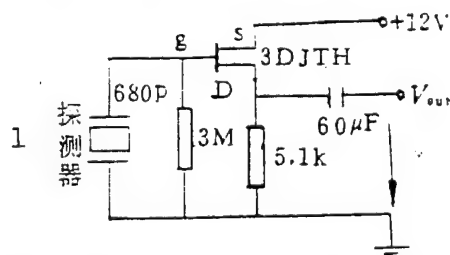


Fig. 5. Equivalent operating circuit in detector

Key: 1 Detector

#### 4. Optical Path Adjustment

During the experiment, the optical path was first adjusted through using He-Ne light, which was then guided into the optical path by aiming the internal focalization telescope at the output mirror center of the CO<sub>2</sub> laser device. After that, the center of the output mirror was aimed at the marking-off plate of the telescope to define the He-Ne light following adjustments. Again, He-Ne light was used to adjust attenuator location and focusing system until focusing flare became a complete circular flare, and finally to adjust detector location.

#### 5. Experiment Reliability Analysis

Factors that affect experiment reliability can be seen as follows: 1. Distortion action of attenuator over light beam; 2. Matching of detector response time with scanning cylinder rotating speed and its synchronization with oscillograph signal; 3. Effect of scanning cylinder wall thickness. The first two problems have been discussed in the previous part of this paper. Virtually, once the cooling measure is taken, and the parameter is properly picked, it is determined that the effect of these two factors on experiment reliability can be ruled out. In the following text, we mainly focus our analysis on the effect of scanning cylinder wall thickness.

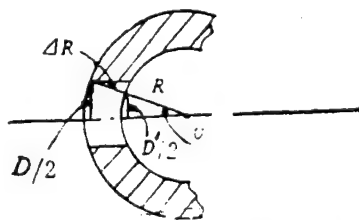


Fig. 6. Analysis of wall thickness effect

Noticing that when hole (11th hole) sitting at the axial

center of the scanning cylinder wall rotates from one side of the flare to the other to form a maximum edge angle, the hole is located at the flare edge. Suppose flare diameter at outer wall is  $D$ , wall thickness is  $\Delta R$ , and outer diameter of scanning cylinder is  $R$  (as indicated in Fig. 6), then the flare diameter on inner wall  $D'$  is:

$$D'/2 = (R - \Delta R) \sin \theta' \approx (R - \Delta R) \cdot \frac{D/2}{R} \quad (2)$$

and light passing area ratio

$$S'/S = \pi (D'/2)^2 / [\pi (D/2)^2] = D'/D \quad (3)$$

Then substituting  $R=40$  mm,  $\Delta R=0.5$  mm,  $D=5$  mm (focusing flare) in above two equations,  $S'/S=0.9875=98.75\%$  can be derived. Obviously, the effect of wall thickness can also be ignored.

### 3. Experiment Result

With foregoing experiment equipment, a measurement was made toward the far-field output laser beam distribution of a 2 KW TE CW CO<sub>2</sub> laser device developed by Laser Research Institute affiliated with Central China University of Science and Engineering. Further, research [3] was conducted of the laser beam quality under different rotating conditions. The result proved that our experiment was a success and our experiment equipment was reliable.

Fig. 7. shows a group of scanning curves and optical field spacial distribution curves after processing (processing method is referred to in Reference [1]). Fig. 8. indicates corresponding flare burn tracks.

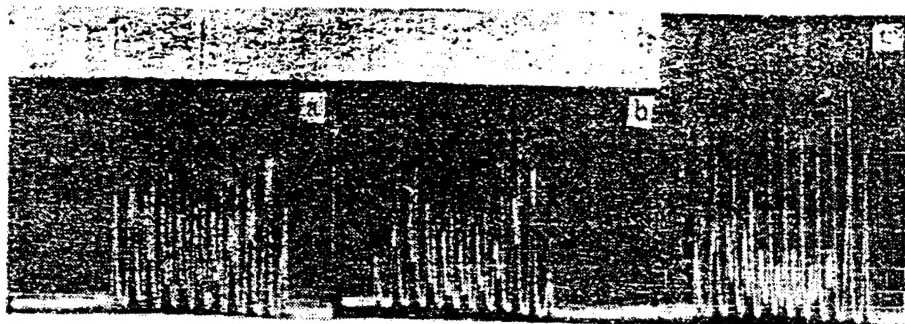


Fig. 7-1. Scanning curves of laser  
beam far-field distribution under  
different output power

Scanning cylinder rotating speed is 400 RPM;  
combined focal length of focusing system is 490 mm

a-- $P_{\text{out}}=1.250$  kW,  $t=5$  ms/cm  
b-- $P_{\text{out}}=1.744$  kW  $t=5$  ms/cm  
c-- $P_{\text{out}}=2.356$  kW  $t=2$  ms/cm



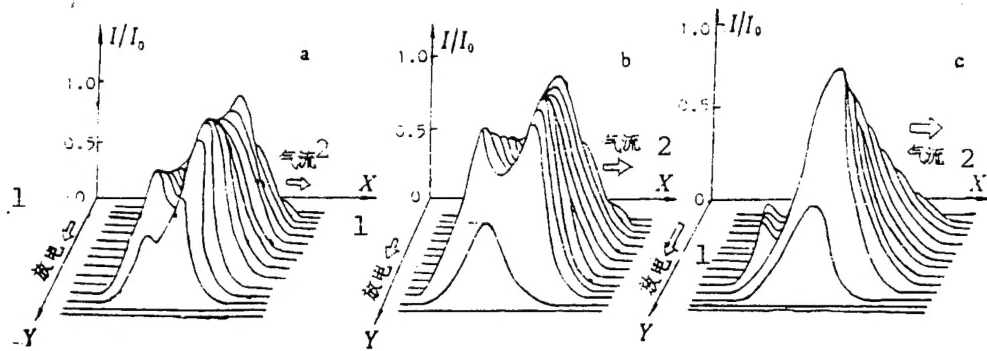


Fig. 7-2. Far-field spatial distribution curves of optical field under different output power  
(corresponding to scanning curves)

Key: 1. Electric discharge; 2. Air current

a-- $P_{\text{out}}=1.250$  kW    Injected electric current  $i=3.5\text{A}$   
 $P_{\text{a}}=8.717$  kW    Corresponding flare No. 119

b-- $P_{\text{out}}=1.744$  kW    Injected electric current  $i=4.5\text{A}$   
 $P_{\text{a}}=12.333$  kW    Corresponding flare No. 121

c-- $P_{\text{out}}=2.356$  kW    Input electric current  $i=6.0\text{A}$

$P_{\text{a}}=15.258$  kW    Corresponding flare No. 124



Fig. 8. Laser flare burn tracks  
corresponding to Fig.7 (burned at  
1.5 m from window surface)

|                        |                             |
|------------------------|-----------------------------|
| a-- $P_{out}=1.250$ kW | Corresponding flare No. 119 |
| b-- $P_{out}=1.744$ kW | Corresponding flare No. 121 |
| c-- $P_{out}=2.356$ kW | Corresponding flare No. 124 |

#### 4. Conclusion

Measurements demonstrate that the two-dimensional scanning method discussed in this paper proves reliable in measuring the far-field intensity distribution of high-power laser beams. It is an indispensable setup for research on laser device operating features and laser beam quality.

Many thanks to Mr. Li Zhaiguang, director of Laser Research Institute affiliated with the Central China University of Science and Engineering, and Prof. Li Shimin for their assistance, as well as all staff members of the High-power CO<sub>2</sub> Laser Device Research Group for their support.

#### References

- [1] "Laser", 1979, Issue 1, P.36-38
- [2] J.A.P., 1974, Vol. 45, No.1, P.350-356
- [3] "China Laser", 1986, Vol.13, Issue 9, P.600

About Author: Jiang lijuan, female, born in May, 1957, is an engineer. She used to engage in research on laser technology, optical fiber telecommunications passive detector. Currently she is working on coherence optical fiber telecommunications.

Date of receiving paper: August 26, 1989

**DISTRIBUTION LIST**

**DISTRIBUTION DIRECT TO RECIPIENT**

**ORGANIZATION**

**MICROFICHE**

|                                  |   |
|----------------------------------|---|
| B085 DIA/RTS-2FI                 | 1 |
| C509 BALL0C509 BALLISTIC RES LAB | 1 |
| C510 R&T LABS/AVEADCOM           | 1 |
| C513 ARRADCOM                    | 1 |
| C535 AVRADCOM/TSARCOM            | 1 |
| C539 TRASANA                     | 1 |
| Q592 FSTC                        | 4 |
| Q619 MSIC REDSTONE               | 1 |
| Q008 NTIC                        | 1 |
| Q043 AFMIC-IS                    | 1 |
| E404 AEDC/DOF                    | 1 |
| E410 AFDTC/IN                    | 1 |
| E429 SD/IND                      | 1 |
| P005 DOE/ISA/DDI                 | 1 |
| 1051 AFIT/LDE                    | 1 |
| PO90 NSA/CDB                     | 1 |

Microfiche Nbr: FTD96C000342  
NAIC-ID(RS)T-0146-96